Hydrothermal Synthesis, X-Ray Structure and Complex Magnetic Behaviour of $Ba_4(C_2O_4)Cl_2[\{Fe(C_2O_4)(OH)\}_4]$

Daniel J. Price,[a, c] Scott Tripp,[e] Annie K. Powell,[a, d] and Paul T. Wood*[a, b]

Dedicated to the memory of Professor Olivier Kahn

Abstract: Hydrothermal reaction of iron(III) chloride, barium chloride and sodium oxalate in a narrow stoichiometry range produces the title compound $Ba_4(C_2O_4)Cl_2[\{Fe(C_2O_4)(OH)\}_4]$ (**1**). This new iron(II) oxalate crystallises in the tetragonal space group $P4_2/mnm$: $a = 13.811(3)$, $c = 7.026(2)$ Å. The structure consists of parallel chains of μ_2-hydroxy-bridged iron(II) ions. These are connected by bridging oxalates to form an anionic framework with large channels that contain the remaining barium, chloride and oxalate counter ions. Magnetisation studies on an oriented single crystal of **1** revealed a magnetic phase transition at 32 K and a strong easy-plane anisotropy at all temperatures. Above T_c the compound behaves as an $S = 2$ XY antiferromagnetic chain, showing a broad maximum in the susceptibility at about 70 K. We determined the intrachain coupling J and the interchain coupling J' to be $-7\ cm^{-1}$ and $\pm 0.4\ cm^{-1}$, respectively. The low-temperature phase is an ordered antiferromagnetic state. Zero- and longitudinal-field muon spin-rotation/relaxation studies support this interpretation; below T_c oscillations in the muon spin-autocorrelation function are observed giving unambiguous evidence for a non-zero sublattice magnetisation and proof of a long-range magnetically ordered state.

Keywords: hydrothermal synthesis · iron · magnetic properties · MuSR · O ligands

Introduction

The search for new molecular-based magnetic materials has shown that such simple ligands as azide,[1] cyanide,[2] dicyanamide[3] and oxalate[4] have structural chemistry of considerable complexity. The attractiveness of these ligands lies both in the fact that they provide good superexchange pathways for magnetic coupling and that they coordinate in predictable ways facilitating a "crystal engineering" approach to synthesis. These anions are commonly combined with ancillary ligands, such as polypyridyls and other multidentate nitrogen heterocycles, in order to achieve a wider range of structural types. The inherent low solubility of coordination network materials makes it difficult in many cases to obtain the product in a microcrystalline form necessary for good characterisation. We have recently shown that solvothermal synthesis is a good way of crystallising molecular-based magnetic materials,[5] particularly when small anions such as oxalate[6] and squarate[7] are used. This approach has several advantages, including the ability to synthesis otherwise unobtainable materials and the possibility to form new materials in which the structure is modified by presence of included small ions, such as halides and Group 1 and 2 cations, within the lattice. In general we are able to prepare materials which are similar to minerals in their density of spin carriers, but which have the structural diversity of conventional molecular-based materials.

[a] Dr. P. T. Wood, Dr. D. J. Price, Prof. A. K. Powell
School of Chemical Sciences, University of East Anglia
Norwich, NR4 7TJ, (UK)
Fax: (+44) 1603-259396
E-mail: p.wood@uea.ac.uk

[b] Dr. P. T. Wood
Present address:
University Chemical Laboratory, University of Cambridge
Lensfield Road, Cambridge, CB2 1EW (UK)

[c] Dr. D. J. Price
Present address:
Department of Chemistry, University of Southampton
Highfield, Southampton, SO17 1BJ (UK)

[d] Prof. A. K. Powell
Present address:
Institut für Anorganische Chemie der Universität Karslruhe
Engesserstrasse Geb. Nr. 30.45, 76128 Karlsruhe (Germany)

[e] S. Tripp
Quantum Design, 11578 Sorrento Valley Road
San Diego, CA 92121-1311 (USA)

Results and Discussion

Synthesis: $Ba_4(C_2O_4)Cl_2[\{Fe(C_2O_4)(OH)\}_4]$ (**1**) was discovered during a systematic study of the hydrothermal chemistry

0947-6539/01/0701-0200 $ 17.50+.50/0

of the ternary system $FeCl_3/Na_2C_2O_4/BaCl_2$. Experiments performed across the whole compositional phase diagram revealed the iron(II) mineral humboldtine, α-$[Fe(C_2O_4)(H_2O)_2]$, to be particularly stable, forming the major solid phase for a very wide range of starting compositions. However, there exists a narrow region in which **1** can be formed exclusively. There are two important features of the synthesis on which we will comment. Firstly, under hydrothermal conditions the aqueous iron(III) ions are reduced to iron(II) in the product. This, along with similar observations of metal reductions in many hydrothermal transition metal/carboxylate[6, 8] reactions, is accounted for by the Nernst equation, which shows how redox potentials are directly related to temperature and the product of the activities of the species involved. Secondly, although no base is employed in the synthesis, the product contains hydroxide ions. Despite the fact that the dissociation constant of water increases with increasing temperature, we believe that (as under ambient conditions) the hydrolysis is facilitated by the iron(III) ions. This contention is supported by the fact that all attempts to prepare **1** starting from $FeCl_2$ were unsuccessful, yielding only humboldtine, thus showing no evidence of hydrolysis and implying that hydrolysis must occur before the reduction of the metal ions. We have previously observed a similar effect[6] in the synthesis of $[Fe_2(OH)_2(C_2O_4)]$.

To date we have been unable to prepare analogues of **1** by replacing iron, barium and chloride with any other transition metal, alkali earth metal or halide, respectively.

Structure: Compound **1** crystallises in the primitive tetragonal space group $P4_2/mnm$. Its structure is comprised of an anionic coordination network with the stoichiometry $Fe(OH)(C_2O_4)$ which contains large cavities occupied by barium, chloride and additional oxalate ions (Figures 1 and 2). This combination of ions appears to be crucial in stabilising this framework structure as no other related combination of ions has produced anything similar. This is not surprising in view of the range of interactions found in **1** which include electrostatic, hydrogen and covalent bonding in addition to steric effects. The network consists of octahedral iron(II) ions bridged by hydroxide and oxalate groups. Each iron atom is coordinated to two hydroxides in a *trans* geometry with the remaining coordination sites occupied by unidentate oxygen atoms from four oxalate anions. The hydroxides are μ^2-bridging to adjacent iron atoms; this leads to the formation of a chain of vertex-sharing FeO_6 polyhedra zig-zaging along the crystallographic *c* axis. The axes of the individual polyhedra are displaced by an angle of 28.8° from the *c* axis (Figure 3). The oxalates which are part of the anionic network each bridge four iron ions, two from one chain and two from an adjacent chain. In this way the chains are linked into a square lattice. There are two types of channel running parallel to the *c* axis. These alternate like the black and white squares on a chessboard. Type-1 channels have concave edges and contain the chloride ions which lie on the 4_2 screw axis. Towards the edges of these channels and on opposite faces are pairs of barium cations providing a tetrahedral environment for the chloride ions which sit at the centre of the channel. The convex type-2 channels are filled with columns of oxalate anions, which coordinate to the barium ions in the neighbouring channels. The anionic network, as well as the barium and chloride ions form an *I*-centred lattice, but this centring is broken by the orientation of the oxalate ions which alternate between neighbouring type-2 channels.

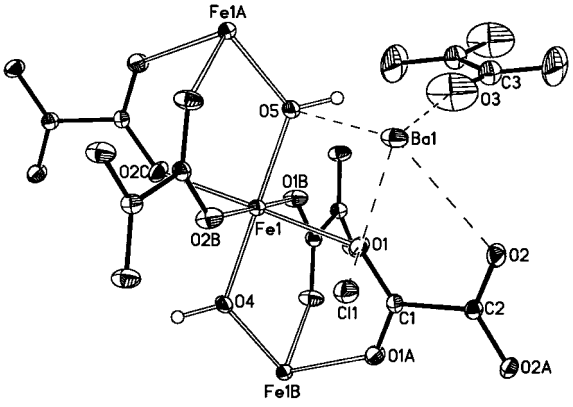

Figure 1. Part of an iron hydroxide oxalate chain of **1** with associated barium, chloride and noncoordinated oxalate ions. Thermal ellipsoids are at the 50% probability level.

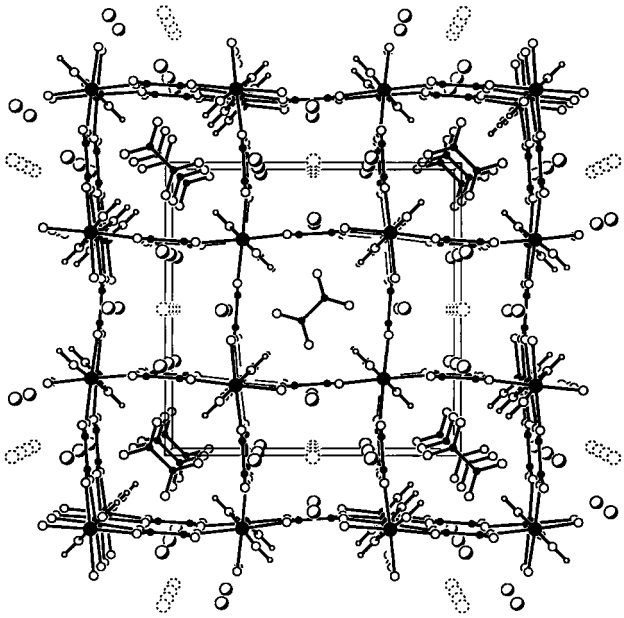

Figure 2. Packing diagram of **1**, viewed along the tetragonal *c* axis, and showing how Fe(OH) chains are held together in a square lattice. Type-1 and type-2 channels can be seen containing barium and chloride ions or oxalate ions, respectively.

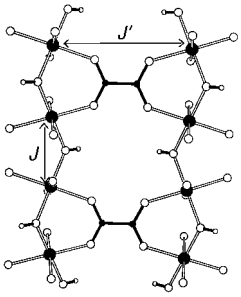

Figure 3. The canted chain structure of vertex-shared "FeO_6" octahedra showing the coordination environment of network oxalate ions and the two superexchange pathways (*J* and *J'*).

The local reduction in symmetry produced by placing the D_{2h} oxalate anion in the square channels of the lattice network is clearly seen in the infrared spectrum of this material. The hydroxy groups of the Fe(OH) chain are directed into the centre of the channels and form two types of bifurcated hydrogen bonds in which one hydroxy, O5H5 points towards the O-C-C-O side of the anion and the other, O4H4 is directed towards the O_2C^- end of the oxalate. Consequently, both the stretching and bending OH modes are split reflecting the two different OH environments.

The iron(II) environment is tetragonally compressed with the two Fe–O (hydroxide) bonds averaging 1.998(2) Å; the average Fe–O (oxalate) bond is 2.214(5) Å. This Jahn–Teller distortion is both predicted and often seen for this ion. The barium ions are nonacoordinate with seven oxygen and two chloride ligands. The Ba–O bond lengths range from 2.574(7) to 3.156(2) Å, while the Ba–Cl bond length is 3.176(6) Å

Magnetism

Powder susceptibility measurements: The paramagnetic susceptibility shows a very broad maximum reaching $3.38 \times 10^{-2}\,cm^3\,mol^{-1}$ at $65(\pm 5)$ K. This behaviour is not well modelled by Curie–Wiess law. Plotting the product χT versus T shows a continuous decrease on cooling, giving strong support for an overall antiferromagnetic exchange interaction. The room temperature moment of 3.45 μ_B per iron ion is well below the value of 4.89 μ_B expected for an isolated $S=2$ iron(II) ion; this suggests that either exchange coupling or zero-field splitting effects are significant even at this temperature.

Single-crystal measurements: The high crystallographic symmetry of **1** means the susceptibility tensor χ_{ij} is uniaxial with its principal axis coincident with the principal crystallographic axis. Thus two independent components $\chi_\parallel$ and $\chi_\perp$ were measured (with an applied field $H=100$ G) parallel and perpendicular to the crystallographic c axis, respectively. Their temperature dependence is shown in Figure 4. The most striking feature is that $\chi_\perp \gg \chi_\parallel$ for all temperatures. On cooling, $\chi_\parallel$ goes through a broad maximum at $70(\pm 5)$ K. No such maximum exists for $\chi_\perp$. At 32 K there is an abrupt change in behaviour marked by discontinuities in $\chi_\perp$ and the gradient

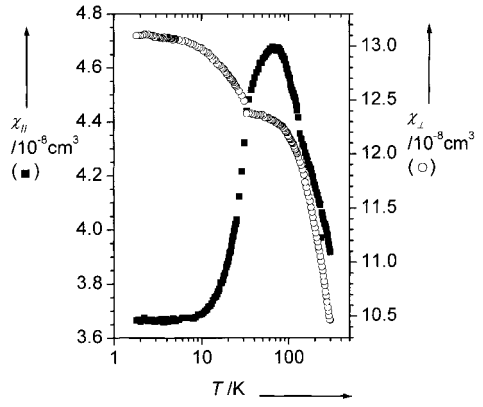

Figure 4. Thermal dependence of the parallel and perpendicular static susceptibilities in an applied field of 100 G.

of $\chi_\parallel$. Below this temperature $\chi_\perp$ rises steeply at first then levels off, while $\chi_\parallel$ after initially decreasing levels off to a non-zero value as T approaches 0 K.

It is clear that there are two magnetic phases. The changes in $\chi_\perp$ and $d\chi_\parallel/dT$ at 32 K are linked to the onset of long-range ordering. This is clearly seen by plotting $d\chi_\parallel T/dT$, which is approximately proportional to the magnetic specific heat capacity.[9] Here a λ-like anomaly at 32 K is indicative of a second-order magnetic phase transition. Thus the high-temperature phase is principally a paramagnetic state, while the low-temperature phase is an antiferromagnetically ordered state. In both phases the magnetic behaviour is complex. The discussion of this behaviour starts from the microscopic perspective of single ion behaviour and then considers the effects of exchange coupling on the observed susceptibility. The octahedral, high-spin iron(II) ions have a large tetragonal compression ($\sim 10\,\%$) which splits the $^5T_{2g}$ state into a lower lying $^5B_{2g}$ orbital singlet and a ^5E_g doublet state. Here the splitting parameter D is positive and we can expect an XY-like single-ion anisotropy in which the ion has an easy-plane of magnetisation with $\mu_\perp > \mu_\parallel$ (for which $\parallel$ and $\perp$ refer to the z axis of the crystal field).[10] It is reasonable to assume that the behaviour of the paramagnetic phase is determined predominantly by the single-ion properties particularly at the highest temperatures (e.g., for $T \sim 10\,T_c$) at which cooperative interactions will be less significant. Using this approximation we can relate the observed magnetisations to the microscopic moments of the iron(II) ions parallel and perpendicular to the local crystal field z axis. This is done by taking the average direction cosines[11] between the local crystal field axis and the applied field. Using the values for $\boldsymbol{M}_\parallel$ and $\boldsymbol{M}_\perp$ ($\boldsymbol{M}$ = magnetisation) at 300 K we obtain a value for the ratio $g_\perp/g_\parallel = 3.9$ (g is the Landé g factor). While it has been noted previously that such XY-like spin anisotropy is more prevalent in uniaxial crystals,[12] in this case it originates from the single-ion properties and not just as a consequence of crystallographic symmetry.

The spin–spin coupling interactions in a molecular-based magnetic material are governed by the superexchange pathways. In **1** there are two types of superexchange pathways that together connect all the ions into a three-dimensional network. The first is the single-atom μ_2-hydroxide bridge (J) and the second is a *trans* oxalate bridge (J') (see Figure 3). The hydroxy-bridged network forms a simple one-dimensional chain with an Fe–Fe separation of 3.513(1) Å, while the oxalate-mediated interactions link an ion to four others in neighbouring chains, Fe···Fe 6.906(2) Å. Together these couplings J and J' form a tetragonally distorted, simple cubic net. In general, shorter bridges mediate stronger superexchange couplings. On this basis the two-bond coupling J should be very much greater than the five-bond pathway of J'. Thus we may expect this system to behave as an array of chains running parallel to the c axis, with a strong intrachain interaction and a much weaker interchain coupling. It has been rigorously shown from thermodynamic arguments that isolated chains cannot sustain long-range order (regardless of any single-ion or exchange anisotropy) because of an inordinate cost in entropy.[9] In such cases there will be no magnetic phase transition above $T = 0$ K.

0947-6539/01/0701-0202 $ 17.50+.50/0 *Chem. Eur. J.* **2001**, *7*, No. 1

The expected behaviour for an antiferromagnetically coupled chain of spins for which the interchain interaction is zero is characterised by a broad maximum in $\chi(T)$ and a non-zero intercept[13] at $T=0$ K. If the interchain interaction is small but finite, as the thermal energy is reduced the effects of the interchain coupling will become more significant and eventually a cross-over from one- to three-dimensional behaviour will occur. This is often marked by a phase transition to a state of long-range order. This is exactly what we observe; on cooling, $\chi_\parallel$ and $\chi_\perp$ have broad features ($\chi_\parallel$ has a distinct maximum at about 70 K) indicative of short-range antiferromagnetic correlations and a one-dimensional character. Further cooling sees a sharp phase transition at 32 K to some form of long-range ordered antiferromagnetic state.

The behaviour of a chain of interacting isotropic spins is given by the Heisenberg Hamiltonian [Eq. (1)] and although this equation is analytically insoluble, certain approximations have allowed the thermodynamic properties to be calculated. Using a classical approach Fisher[14] has derived Equation (2a).

$$H=-2\Sigma_i \mathbf{S}_i\cdot\mathbf{S}_{i+1} \tag{1}$$

$$\chi_\parallel=\frac{Ng^2\mu_B^2S(S+1)}{3k_BT}\left(\frac{1+u}{1-u}\right) \tag{2a}$$

$$u=\coth[2JS(S+1)/k_BT]-k_BT[2JS(S+1)]^{-1} \tag{2b}$$

After adding a constant term to account for the Van Vleck temperature-independent contribution to the paramagnetism[15] a reasonable least-squares fit was obtained for $\chi_\parallel$ in the range $32=T=300$ K, with $J=-7.6(2)$ cm^{-1}. In an alternative method Weng[16] has used numerical methods to determine the behaviour of a quantum spin $S=2$ antiferromagnetic chain. This is approximated by the polynomial expansion subsequently published by Hatfield[17] [Eq. (3), in which $A=2.0000$, $B=71.938$, $C=10.482$ and $D=955.56$].

$$\chi_\parallel=\frac{Ng^2\mu_B^2}{k_BT}\left[\frac{A+B(|J|k_BT)^2}{1+C(|J|k_BT)+D(|J|k_BT)^3}\right] \tag{3}$$

After adding a temperature-independent component this equation gave a superior fit (Figure 5) yielding a value of $J=-6.3(2)$ cm^{-1}. The behaviour of **1** deviates from these models in two important respects. Firstly, the shape of $\chi_\parallel$ is not mirrored by $\chi_\perp$. Secondly, $\chi_\parallel$ shows a slight deviation from the model across the whole temperature range. At the lowest temperatures (as T approaches T_C) this discrepancy may be accounted for by the onset of interchain interactions. While deviations at higher temperatures could be due to our simplified choice of model, it is clear that at the very least a planar Heisenberg model is required. With respect to the low-temperature deviations, similar systems have previously been modelled by combining these equations with a mean-field term to account for the interchain interactions.[15, 18] This did not significantly improve the quality of the fit in the present case. We can however deduce a value for the interchain interaction by employing Oguchi's method[19] which relates T_c, S and $|J|$ to $|J'|$. This method is particularly successful when the coupling ratio η (equal to $|J'|/|J|$) is small. Thus we obtain $\eta\approx0.063$ and $|J'|\approx0.4$ cm^{-1}.

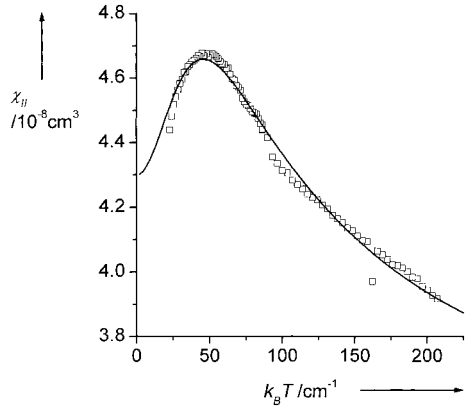

Figure 5. The best-fit curve (solid line) of Weng's expression for an antiferromagnetically coupled spin 2 chain [Eq. (3)—see main text].

Single-crystal susceptibility measurements allow us to determine the anisotropy, a useful quantity in interpreting the magnetic behaviour. The anisotropy for a uniaxial material is given by Equation (4).

$$A=\frac{(\chi_\perp-\chi_\parallel)}{(\chi_\perp+\chi_\parallel)} \tag{4}$$

Here (in a paramagnetic state) if the magnetic moments are rigorously confined to the perpendicular plane then $A=+1$, if the moments are constrained to the unique axis then $A=-1$ and if there is no preferential orientation for the moments then $A=0$. These extreme scenarios correspond to the XY, Ising and Heisenberg models, respectively. For real systems at finite temperatures we can expect intermediate values of A. The temperature dependence of the anisotropy of **1** is shown in Figure 6. The sample displays an easy plane of magnetisation for all temperatures; however, there are significant changes in the value of A over the measured temperature range. A qualitative interpretation can be achieved by considering appropriate sources of anisotropy.

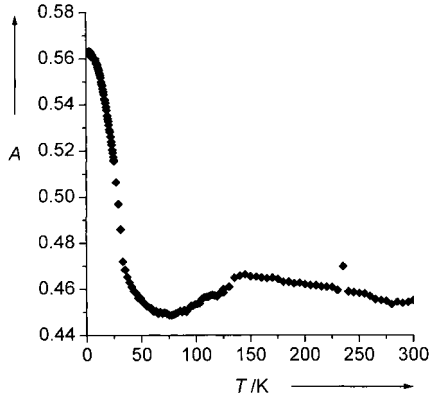

Figure 6. The thermal dependence of the anisotropy, as defined in Equation (4).

Firstly there is an inherent contribution from the single-ion properties. The combined action of spin-orbit coupling and a reduced crystal-field symmetry (tetragonal compression) splits an otherwise degenerate ground-state manifold. As the temperature is lowered the effective g values will

approach those of the single-ion ground state. A second cause of anisotropy derives from the spin–spin interaction. To completely describe the coupling of two spin vectors ($\boldsymbol{S}_i$ and $\boldsymbol{S}_j$) a coupling tensor $\boldsymbol{J}_{ij}$ is required. While symmetry may constrain certain elements of $\boldsymbol{J}_{ij}$,.it is always possible to deconvolute a third-order second-rank tensor into three component parts, such that $\boldsymbol{J}_{ij} = J\boldsymbol{E} + \boldsymbol{D}_{ij} + \boldsymbol{d}_{ij}$ (where $\boldsymbol{E}$ is a unit tensor). Here J is the isotropic exchange, $\boldsymbol{D}_{ij}$ is the symmetric anisotropic exchange interaction, which determines the preferred axis of orientation of the aligned spins, and $\boldsymbol{d}_{ij}$ is the antisymmetric exchange term (the Dzialoshinski–Moriya term), which stabilises non-collinear spin configurations. Both $\boldsymbol{D}_{ij}$ and $\boldsymbol{d}_{ij}$ represent non-Heisenberg exchange interactions.[20] Such non-Heisenberg exchange contributions can be caused by spin–orbit couplings in transition metal systems or by inherently anisotropic dipole–dipole interactions.

In a magnetically ordered phase the dominant cause of anisotropy derives from the anisotropic internal fields associated with each sublattice magnetisation. In this way the ordered state reinforces certain spin orientations making a perturbation much more difficult. This is demonstrated by a classical two-sublattice antiferromagnet, for which induction of a magnetic moment along the principal axis of the spins is energetically much more difficult than in the perpendicular direction, resulting in apparent XY-like anisotropy with $\chi_\perp > \chi_\parallel$.

With these ideas in mind we can qualitatively account for the changes in anisotropy. On cooling, the increase in A corresponds to an increase in XY-character; we attribute this to the single-ion anisotropy which we know is large. The anisotropy reaches a local maximum at 140 K and then decreases below this temperature. This corresponds approximately to the region where the intrachain coupling $\boldsymbol{J}_{ij}$ becomes the dominant interaction. The decrease in A must be equated with a tendency for the anisotropic component of the coupling ($\boldsymbol{D}_{ij}$) to align the spins along the chain direction. As we continue to cool the sample, the anisotropy reaches a minimum at 75 K and then begins to increase. The rate of increase reaches a maximum at the phase transition after which it levels off to a constant value in the low-temperature antiferromagnetic phase. The enhancement of the anisotropy below T_C must be due to the anisotropy of the internal fields in this ordered phase. In the region around T_C it is not clear to what extent each of the sources of anisotropy is contributing to the overall behaviour and consequently the overall spin configuration remains ambiguous.

The magnetisation as a function of the applied field for both parallel and perpendicular orientations (Figure 7) show no dramatic differences on either side of T_C. For $\boldsymbol{M}_\parallel$ we see an exceptionally linear relationship with intercepts at the origin. Such a high degree of linearity is typical of antiferromagnetism. It seems that although at 40 K the phase is not magnetically ordered the strong intrachain coupling results in an antiferromagnetic character. For the perpendicular orientation there is even less apparent difference in the magnetisation curves at 20 and 40 K. The shape of the curve is a little more unusual and bears some of the hallmarks of canted antiferromagnetism. Initially $\boldsymbol{M}_\perp$ rises steeply and then at higher fields ($\boldsymbol{H} > 1000$ G) settles down to a linear relationship of the form $\boldsymbol{M}_\perp = \boldsymbol{M}_0 + \chi\boldsymbol{H}$. The interpretation of the quantities $\boldsymbol{M}_0$ and χ is not clear, as the sample is not a simple canted antiferromagnet. $\boldsymbol{M}_0$ is not a spontaneous magnetisation, but corresponds to a spin configuration that is more easily obtained. Once this configuration has become saturated the more usual linear relationship between $\boldsymbol{M}$ and $\boldsymbol{H}$ takes over.

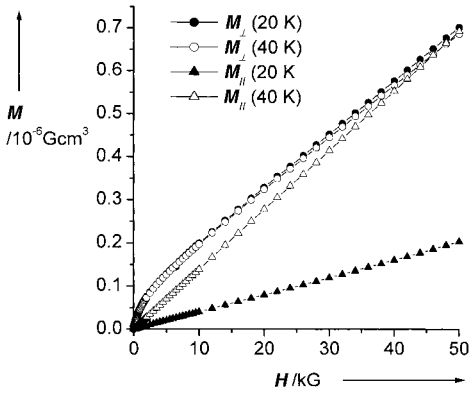

Figure 7. Single-crystal field-dependent magnetisation curves for parallel and perpendicular orientations with measurements made above and below the magnetic phase transition.

Single-crystal magnetic studies are of vital importance in interpreting the behaviour of magnetic systems. This is particularly so for molecular-based materials in which complex structures are built from metal ions usually in low symmetry environments. In the present system the high crystallographic symmetry considerably simplifies the process of performing single-crystal magnetisation measurements. The utility of this approach is immediately clear as the magnetic phase transition and large XY anisotropy are not evident in measurements on powder samples. Most aspects of the observed behaviour have been successfully rationalised from structural considerations. From a microscopic perspective the distortion from octahedral geometry around the iron ion leads to XY spin anisotropy, whilst the crossover in magnetic lattice dimensionality at the phase transition fits perfectly with that expected from a consideration of the couplings within the structure.

Muon spin-rotation/relaxation (MuSR) studies: MuSR is a very useful and sensitive probe of magnetic and dynamic behaviour.[21] In the experiment positive muons are implanted into the sample with 100% spin polarisation. The muon decay ($\tau_\mu = 2.2$ μs) into a positron is mediated by a parity-violating weak interaction, the effect of which is to cause an enhanced positron emission in the direction of the muon spin at the moment of decay. By measuring the spatial and temporal distribution of the emitted positrons we can deduce the evolution of the muon spin polarisation with time. In the longitudinal geometry used here this means counting positrons in the forward $N^+(t)$ and backward $N^-(t)$ direction. The asymmetry of the polarisation is given as $CG_z(t) = [N^+(t) - \alpha N^-(t)]/[N^+(t) + \alpha N^-(t)]$, where C is a normalisation constant, α is an experimental parameter to correct for different efficiencies of the forward and backward detectors and $G_z(t)$ is the normalised muon spin autocorrelation function.

0947-6539/01/0701-0204 $ 17.50+.50/0 *Chem. Eur. J.* **2001**, *7*, No. 1

The results of zero-field experiments are shown in Figure 8. Above 32 K the depolarisation shows a complex form; it is not satisfactorily fit by either simple Gaussian or Lorentzian decay function but appears to have intermediate behaviour. In paramagnetic materials the electronic spin fluctuations normally occur on too rapid a time scale to provide an increase significantly so that at 33 K it is $\sim 0.55\ \mu s^{-1}$ (Figure 9). At high temperatures spin fluctuations are rapid, cooling slows these fluctuations down and their efficiency in depolarising the muon spin is increased giving an increase in the dynamic depolarisation rate. This interpretation is supported by the 50 G longitudinal field measurements at which the

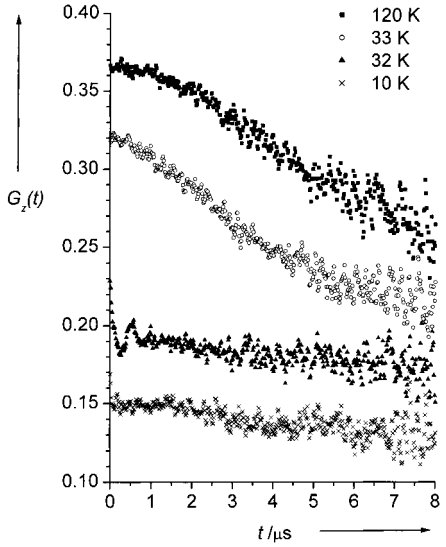

Figure 8. A waterfall plot of the zero-field muon depolarisation curves at selected temperatures. Whilst the scale is correct for the data at 10 K, all other plots are vertically shifted for clarity.

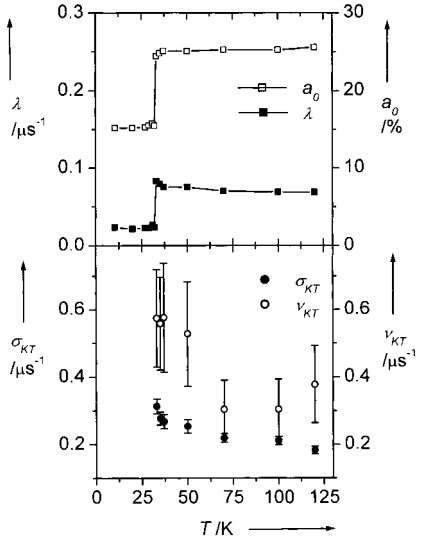

Figure 9. The thermal dependence of the muon spin-relaxation parameters; a_0 is the initial asymmetry, λ is the overall damping factor, σ_{KT} and ν_{KT} are the static and dynamic components of the Kubo–Toyabe model.

effective depolarisation mechanism. If the sample possesses nuclei with non-zero nuclear moments the relaxation may be effected by the distribution of fields caused by the random orientation of the nuclear spins. Nuclear spin relaxation rates are very much longer than the muon lifetime and so have a static distribution of internal fields. Larmor precession of the muon in a range of fields quickly leads to spin relaxation by a dephasing of the muon spin polarisation. In **1** we believe the ^{1}H nuclei provide the largest component to the static random fields experienced by the muons. This is in part due to their close proximity to the likely muon implantation sites. A distribution of static fields results in a longitudinal depolarisation curve $G_z(t)$ with the static Kubo–Toyabe form. Such a curve is characterised by an initial Gaussian-like decay and subsequent recovery should occur at longer times to 1/3 of its initial asymmetry. We do not observe this recovery, but do see a mixture of Gaussian behaviour at short times and exponential decay at longer times suggesting a dynamic component to the muon spin relaxation. The zero-field data can be well fitted with the dynamic form of the Kubo-Toyabe function,[22] for which $\sigma/\nu \sim 0.5$ (σ is the static component of the relaxation and is related to the distribution of internal fields caused by non-zero nuclear moments and ν is effectively a muon hop rate). In this model the dynamic component is based on a "strong collision theory" for muon diffusion (hopping). This is not an ideal description of electronic spin fluctuations, nevertheless in the absence of other models we believe that the dynamic Kubo–Toyabe model at least provides a useful parameterisation. At 120 K the hop rate is $\sim 0.3\ \mu s^{-1}$. On cooling below 60 K this dynamic component is seen to Gaussian character of the relaxation function is completely suppressed. This external field decouples the static nuclear and dynamic electronic components, since it is much larger than the dipolar nuclear fields but small enough not to perturb significantly the dynamic electronic behaviour. Hence these depolarisation curves are well modelled with a slowly decaying Lorentzian function. The very slow nature of the muon spin relaxation (a loss of $\sim 15\,\%$ of the initial asymmetry after 15 μs) results in a large error associated with the relaxation rate, nevertheless the values obtained are comparable with the rates obtained from the zero-field experiments.

Between 33 and 32 K there is a great change in the evolution of the muon depolarisation curve (Figure 8). At 32 K the Gaussian component is lost, the value of the initial asymmetry has decreased (Figure 9) and most strikingly a damped oscillatory component is evident (Figure 10). This behaviour, seen in other molecular magnets[23] is unambiguous proof of a phase transition to a magnetically ordered commensurate phase where the observed oscillations are due to Larmor precession of implanted muons in the internal magnetic field. Since the Larmor frequency can be simply related to the magnetic field strength by $\omega_L = \gamma_\mu \boldsymbol{H}$, in which γ_μ is the magnetogyric constant for the muon (135 MHz T^{-1}), the thermal evolution of the oscillation frequency is a direct measure of the evolution of the internal field at the muon site. That we only observe one oscillation frequency suggests that there is one site for the implanted muon or that at least there is only one site for which the internal field is within the measurable range for this experiment. From a chemical perspective this is expected to be on O3, the coordinately least

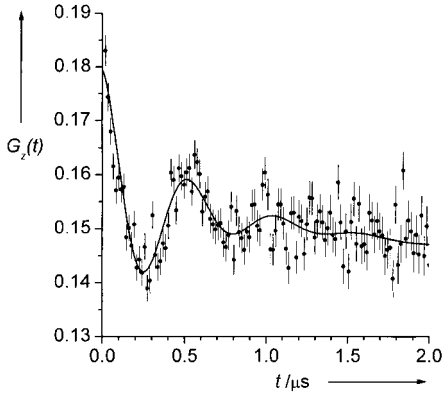

Figure 10. Best fit for the oscillatory component at $T = 31$ K; unambiguous evidence of Larmor precession and the existence of a non-zero mean value for the internal field at the muon site.

saturated oxygen on the isolated oxalate within the type-2 channels. The thermal dependence of the oscillation frequency and thus of the internal field is shown in Figure 11 along with the predicted behaviour from mean field theory.

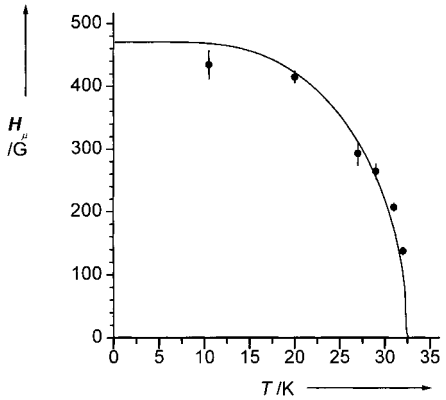

Figure 11. Calculated thermal evolution of the magnetic field experienced by the muon from the oscillation frequencies below T_c. Also shown (solid line) is the mean-field theory prediction.

Conclusion

This work reports the synthesis, crystal structure and magnetic behaviour of a new iron(II) oxalate compound. Compound **1** was discovered during a systematic study of the hydrothermal reactions of $FeCl_3/Na_2C_2O_4/BaCl_2$ system. Compound **1** appears to crystallise in an *I*-centred tetragonal unit cell; however, alternate orientations of the oxalate within the channels breaks this symmetry resulting in a primitive lattice. The structure has a very strong one-dimensional character with vertex-sharing FeO_6 polyhedra connected into chains that run parallel to the *c* axis. The magnetic behaviour of **1** is surprisingly complex, in that even a qualitative explanation requires many aspects of magnetochemistry to be considered. It is clear from the susceptibility studies and zero-field MuSR experiments that **1** has a magnetic phase transition at 32 K. Above this temperature the behaviour is of an antiferromagnetically coupled spin 2 chain. The large positive single-ion anisotropy has, on average, its axis parallel to the chain, thus the spins are confined perpendicular to the chain direction. Using appropriate available models we derive the intrachain coupling, J and the interchain coupling, J' to be -7 and ± 0.4 cm^{-1}, respectively. This value of J' is quite large for such a separation between iron ions, and it is likely that it contains a significant dipolar contribution, particularly in view of the probable spin orientations. In the three-dimensional antiferromagnetically ordered phase MuSR studies provide a direct measure of the thermal evolution of the sublattice magnetisation. In conjunction with complimentary neutron diffraction experiments currently underway this data will help us deduce the ground-state structure of the antiferromagnetic phase. This molecular-based material provides a rare and useful example of a spin 2 material with planer anisotropy. Such a system provides an excellent opportunity to see how the interplay of various forms of magnetic anisotropy conspire to control its behaviour.

Experimental Section

Infrared spectra were recorded on a Nicolet Impact 410 FTIR spectrometer as KBr pellets. C, H, N and Cl analysis was determined by the UEA analytical service. All chemicals were used as received without further purification.

Tetrabarium dichloride oxalate tetra[iron(II)hydroxyoxalate] (1): Sodium oxalate (261 mg, 1.95 mmol) and barium chloride dihydrate (780 mg, 3.20 mmol) were added to a solution of iron(III) chloride hexahydrate (312 mg, 1.16 mmol) in distilled water (10 mL). The reaction mixture was placed in a 23 cm^3 Teflon-lined autoclave and heated to 220 °C for 100 hours, then cooled back to room temperature. Filtration gave golden-yellow needles of the product (yield: 160 mg, 0.24 mmol, 41 %). Elemental analysis calcd (%) for $Ba_4Fe_4Cl_2C_{10}O_{24}H_4$: C 8.86, H 0.30, Cl 5.25; found C 8.79, H 0.26, Cl 4.35; IR (Kbr): $\tilde{\nu}$ 3370 (s, br, OH), 3234 (s, br, OH), 2918 (w), 2763 (w), 1625 (vs, br, C=O), 1359 (m), 1317 s, 925 (m, br, OH), 844 (m, br, OH), 780 (s), 756 (w), 503 (m), 466 cm^{-1} (w).

Tetrabarium dichloride oxalate tetra[iron(II)deuteroxyoxalate]: The deuterated analogue can be formed by using the same molar ratios of anhydrous reagents and reacting in D_2O. IR (KBr): $\tilde{\nu}$ 2921 (vw), 2852 (vw), 2506 (m, br, OD), 2411 (m, br, OD), 1634 (vs, br, C=O), 1361 (m), 1317 (s), 807 (w), 780 (s), 710 (m, OD), 623 (m, OD), 527 (m), 493 (m), 472 (m), 458 cm^{-1} (m).

X-ray crystallography: $Ba_4(C_2O_4)Cl_2[\{Fe(C_2O_4)(OH)\}_4]$ crystallises as orange-yellow needles. The room temperature data were collected from a fragment with dimensions $0.16 \times 0.04 \times 0.04$ mm on a Rigaku R-axis II image plate diffractometer equipped with a rotating anode X-ray source with graphite monochromated $Mo_{K\alpha}$ radiation ($\lambda = 0.71073$ Å). A series of 45 ϕ oscillation photographs were measured ($\Delta\phi = 5°$) with a crystal to detector distance of 69 mm, giving data to a resolution of 0.76 Å. Cell dimensions were obtained by refinement of 105 reflections in the range $8.88 \leq 2\theta \leq 55.76°$ from a single frame. Full details of the data collection are given in Table 1. The data were indexed and scaled by using the programs DENZO and SCALEPACK. The structure was solved by direct methods and the positions of subsequent atoms obtained from Fourier difference maps. All non-hydrogen atoms were refined anisotropically by a full-matrix least-squares on F^2. Hydrogen atoms were added in calculated positions and refined by using a riding model. Solution and refinement was performed with SHELXTL software. Fractional atomic coordinates and equivalent isotropic thermal parameters are displayed in Table 2, while selected bond lengths and angles are given in Table 3. Crystallographic data (excluding structure factors) for the structures reported in this paper have been deposited with the Cambridge Crystallographic Data Centre as supplementary publication no. CCDC-146191. Copies of the data can be obtained free of charge on application to CCDC, 12 Union Road, Cambridge CB2 1EZ, UK (fax: (+44) 1223-336-033; e-mail: deposit@ccdc.cam.ac.uk).

0947-6539/01/0701-0206 $ 17.50+.50/0 *Chem. Eur. J.* **2001**, *7*, No. 1

Table 1. Crystallographic information for compound **1**.

formula	$Fe_2Ba_2ClC_5O_{12}H_2$
M_w	675.90 g mol^{-1}
crystal system	tetragonal
space group	$P4_2/mnm$ (no. 136)
a [Å]	13.811(3)
c [Å]	7.026(2)
V [Å^3]	1340.2(6)
Z	4
ρ_{calcd} [g cm^{-1}]	3.350
$F(000)$	1236
crystal size [mm]	$0.16 \times 0.04 \times 0.04$
θ range [°]	2.09–28.34
index range	$-17 \le h \le 17$
	$-18 \le k \le 18$
	$-9 \le l \le 9$
reflections collected	10527
independent reflections	946
R_{int}	0.0798
data/parameters	944/64
$R1$ [$I > 2\sigma(I)$]	0.0395
$wR2$ [all data]	0.1464
goodness-of-fit, S	1.122
largest peak/hole [e Å^{-3}]	1.979/ – 2.536

Table 2. Fractional atomic coordinates and average displacement parameters. U_{eq} is defined as one third of the trace of the othoganalized U_{ij} tensor.

	x	y	z	U_{eq}
Ba(1)	0.4964(1)	0.1916(1)	0	29(1)
Fe(1)	0.7415(1)	0.2585(1)	0.2502(1)	17(1)
Cl(1)	0.5	0	0.25	27(1)
O(1)	0.5896(2)	0.2398(2)	0.3413(4)	29(1)
O(2)	0.3948(2)	0.2274(2)	0.3407(4)	29(1)
C(1)	0.5490(4)	0.2387(4)	0.5	19(1)
C(2)	0.4360(4)	0.2313(4)	0.5	19(1)
O(3)	0.4861(5)	0.3777(5)	0	88(3)
C(3)	0.4613(4)	0.4613(4)	0	31(2)
O(4)	0.7904(3)	0.2096(3)	0.5	27(1)
H(4)	0.8380(3)	0.1620(3)	0.5	32(1)
O(5)	0.6921(3)	0.3079(3)	0	24(1)
H(5)	0.6445(3)	0.3555(3)	0	29(1)

Table 3. Selected bond lengths [Å] and angles [°].

Fe1–O1	2.209(3)	Ba1–O1	2.802(3)	Fe1–O2	2.219(3)
Ba1–O2	2.819(3)	Fe1–O4	1.998(2)	Ba1–O3	2.574(7)
Fe1–O5	2.006(3)	Ba1–O4	3.156(2)	Ba1–O5	3.1438(14)
C1–C2	1.563(8)	Ba1–Cl1	3.1761(6)	C1–O1	1.249(3)
C2–O2	1.257(3)	C3–C3A	1.51(2)	C3–O3	1.205(8)
O4-Fe1-O5	179.8(2)	O1-C1-O1A	126.5(5)	O1-Fe1-O2	83.61(13)
O1-C1-C2	116.7(2)	O1-Fe1-O1A	97.9(2)	O2-C2-O2a	125.8(5)
Fe1-O4-Fe1A	122.9(3)	O2-C2-C1	117.1(2)	Fe1-O5-Fe1A	122.4(3)
O3-C3-O3A	123.0(10)	O3-C3-C3A	118.5(5)		

Magnetic susceptibility measurements: Single-crystal and powder magnetic susceptibility measurements were performed on a Quantum Design MPMS SQUID magnetometer. The diamagnetic contribution to the susceptibility was calculated from Pascal's constants[24] to be -189×10^{-6} cm^3 mol^{-1}. The orientated single-crystal experiments were performed on a square prism with approximate dimensions of $0.40 \times 0.15 \times 0.15$ mm. This was attached to a fine cotton fibre with a small amount of Apezion K grease so that the long axis was parallel to the fibre. The orientation of the crystal and fibre was fixed in a polythene straw, such that the long axis was a) parallel to the applied field and then b) perpendicular. The induced magnetisation was measured parallel to the applied field. Temperature-dependant measurements were made in a field of 100 G from 1.7 to 300 K and field dependent measurements made between 0 and 5.5 T at 20, 30 and 40 K.

MuSR experiments: Muon spin rotation/relaxation experiments were performed on the MuSR instrument at the ISIS facility of the Rutherford–Appleton Laboratory. A finely ground sample of **1** weighing approximately 5 g was lightly pressed into an aluminium mount and held in place with a Mylar film window. The aluminium holder was then masked from the muon beam by a silver plate leaving a sample target with diameter 2.2 cm and a depth of 2 mm. The sample was mounted in a ^{4}He cryostat and placed in the MuSR instrument in the longitudinal geometry. Zero- and longitudinal-field measurements were taken over a range of temperatures from 10 to 120 K. In the case of zero-field measurements the background contribution from the Earth and other extraneous sources in the experiment hall were compensated for by a set of orthogonal Helmholtz coils. A 20 G transverse field measurement was also performed on a standard silver sample for instrument calibration purposes.

Acknowledgement

We thank the EPSRC for funding and Dr C. A. Scott (ISIS) for his assistance with the MuSR measurements.

[1] a) R. Vicente, A. Escuer, J. Ferretjans, H. Stoeckli-Evans, X. Solans, M. Font-Bardía, *J. Chem. Soc. Dalton Trans.* **1997**, 167; b) M. Montfort, J. Ribas, X. Solans, M. Font-Bardía, *Inorg. Chem.* **1996**, *35*, 7633; c) G. De Munno, T. Poerio, G. Viau, M. Julve, F. Lloret, Y. Journaux, E. Rivière, *Chem. Commun.* **1996**, 2587.
[2] a) O. Kahn, J. Larionova, L. Ouahab, *Chem. Commun.* **1999**, 952; b) S. Ferlay, T. Mallah, R. Ouahes, P. Veillet, M. Verdaguer, *Inorg. Chem.* **1999**, *38*, 229; c) S. Ferlay, T. Mallah, R. Ouahes, P. Veillet, M. Verdaguer, *Nature* **1995**, *378*, 701; d) S. Ferlay, T. Mallah, J. Vaissermann, F. Bartolomé P. Veillet, M. Verdaguer, *Chem. Commun.* **1996**, 2481.
[3] a) J. L. Manson, C. R. Kmety, A. J. Epstein, J. Miller, *Inorg. Chem.* **1999**, *38*, 2552; b) J. L. Manson, C. D. Incarvito, A. L. Rhingold, J. S. Miller, *J. Chem. Soc. Dalton Trans.* **1998**, 3705.
[4] a) C. J. Nuttall, P. Day, *Chem. Mater.* **1998**, *10*, 3050; b) P. Day, *J. Chem. Soc. Dalton Trans.* **1997**, 701; c) H. Tamaki, Z. J. Zhong, N. Matsumoto, S. Kida, M. Koikawa, N. Achiwa, Y. Hashimoto, H. Okawa, *J. Am. Chem. Soc.* **1992**, *114*, 6974; d) G. De Munno, M. Julve, F. Nicolo', F. Lloret, J. Faus, R. Ruiz, E. Sinn, *Angew. Chem.* **1993**, *105*, 588; *Angew. Chem. Int. Ed. Engl.* **1993**, *32*, 613; e) G. Antorrena, F. Palacio, M. Castro, R. Pellaux, S. Decurtins, *J. Magn. Magn. Mater.* **1999**, *197*, 581; f) R. Pellaux, H. W. Schmalle, R. Huber, P. Fischer, T. Hauss, B. Ouladdiaf, S. Decurtins, *Inorg. Chem.* **1997**, *36*, 2308; g) S. Decurtins, H. W. Schmalle, R. Pellaux, P. Schneuwly, A. Hauser, *Inorg. Chem.* **1996**, *35*, 1451.
[5] S. O. H. Gutschke, D. J. Price, A. K. Powell, P. T. Wood, *Angew. Chem.* **1999**, *111*, 1158; *Angew. Chem. Int. Ed.* **1999**, *38*, 1088.
[6] a) M. Molinier, D. J. Price, P. T. Wood, A. K. Powell, *J. Chem. Soc. Dalton Trans.* **1997**, 4061; b) D. J. Price, F. Lionti, R. Ballou, P. T. Wood, A. K. Powell, *Phil. Trans. R. Soc. London A* **1999**, *357*, 3089.
[7] D. S. Yufit, D. J. Price, S. O. H. Gutschke, P. T. Wood, A. K. Powell, J. A. K. Howard, *Chem. Commun.* **1999**, 1561.
[8] A. Distler, D. L. Lohse, S. C. Sevov, *J. Chem. Soc. Dalton Trans.* **1999**, 1805.
[9] L. J. deJongh, A. R. Miedema, *Adv. Phys.* **1974**, *23*, 1.
[10] S. Mitra, *Prog. Inorg. Chem.* **1977**, *22*, 309.
[11] a) J. T. Schriempf, S. A. Friedberg, *Phys. Rev. A* **1964**, *136*, 518; b) N. Uryû, *Phys. Rev. A* **1964**, *136*, 527.
[12] R. L. Carlin, *Magnetochemistry*, Springer, Heidleberg, **1986**.
[13] This is ignoring possible quantum phase behaviour and the possibility of Haldane states at extremely low temperature, as this is not relevant to this particular material.
[14] M. E. Fisher, *Am. J. Phys.* **1964**, *32*, 343.
[15] C. J. O'Conner, *Prog. Inorg. Chem.* **1982**, *29*, 203.
[16] C. Y. Weng, Ph.D. Thesis, Carnegie-Mellon University, **1969**.

  0947-6539/01/0701-0207 $ 17.50+.50/0

[17] W. Hiller, J. Strähle, A. Datz, M. Hanack, W. E. Hatfield, L. E. ter Haar, P. Gütlich, *J. Am. Chem. Soc*. **1984**, *106*, 329.
[18] C. S. Hong, Y. Do, *Inorg. Chem*. **1997**, *36*, 5684.
[19] T. Oguchi, *Phys. Rev.* **1964**, *133*, A1089.
[20] "Molecular Magnetism: From Molecular Assemblies to the Devices", J. M. Clemente, A. V. Palii, B. S. Tsukerblat, R. Georges, *NATO ASI Ser. E* **1996**, *321*, 85.
[21] a) S. J. Blundell, *Contemp. Phys.* **1999**, *40*, 175; b) J. Chappert, R. I. Grynszpan, *Muons and Pions in Materials Research*, Elsevier, Amsterdam, **1984**; c) A. Schenck, *Muon Spin Rotation Spectroscopy: Principles and Applications in Solid-State Physics*, Adam Hilger, Bristol, **1985**.
[22] R. S. Hayano, Y. J. Uemura, J. Imazato, N. Nishida, T. Yamazaki, R. Kubo, *Phys. Rev. B* **1979**, *20*, 850.
[23] a) J. L. García-Muñzo, J. Cirujeda, J. Veciana, S. F. J. Cox, *Chem. Phys. Lett.* **1998**, *293*, 160; b) S. J. Blundell, T. Sugano, P. A. Pattenden, F. L. Pratt, R. M. Valladares, K. H. Chow, H. Uekusa, Y. Ohashi, W. Hayes, *J. Phys. Condens. Matter* **1996**, *8*, L1; c) S. J. Blundell, P. A. Pattenden, F. L. Pratt, R. M. Valladares, T. Sugano, W. Hayes, *Europhys. Lett*. **1995**, *31*, 573.
[24] See for example; O. Kahn, *Molecular Magnetism*, VCH, Weinheim, **1993**.

Received: June 28, 2000 [F2574]

  0947-6539/01/0701-0208 $ 17.50+.50/0